

Modelling and Shadowgraph Imaging of Cocrystal Dissolution and Assessment of *In Vitro* Antimicrobial Activity for Sulfadimidine/4-Aminosalicylic Acid Cocrystals

Dolores. R. Serrano¹, Tim Persoons², Deirdre M. D'Arcy¹, Carolina Galiana³, Maria Auxiliadora Dea-Ayuela³, Anne Marie Healy^{1,*}

¹School of Pharmacy and Pharmaceutical Sciences, Trinity College Dublin, Dublin 2, Ireland.

²Department of Mechanical and Manufacturing Engineering, Trinity College Dublin, Dublin 2, Ireland.

³Departamento de Farmacia, Facultad de Ciencias de la Salud, Universidad Cardenal Herrera-CEU, Moncada, Valencia, 46113, Spain.

*Corresponding author:

Tel.: +353 1 896 1444; fax: +353 1 896 2810.

E-mail address: healyam@tcd.ie (A.M. Healy)

Abstract

Purpose: The aim of this work was to evaluate the influence of crystal habit on the dissolution and *in vitro* antibacterial and antiprotozoal activity of sulfadimidine:4-aminosalicylic acid cocrystals.

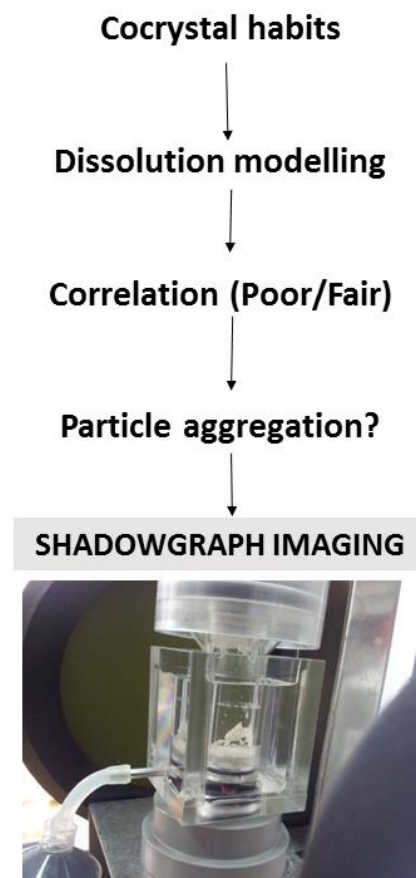
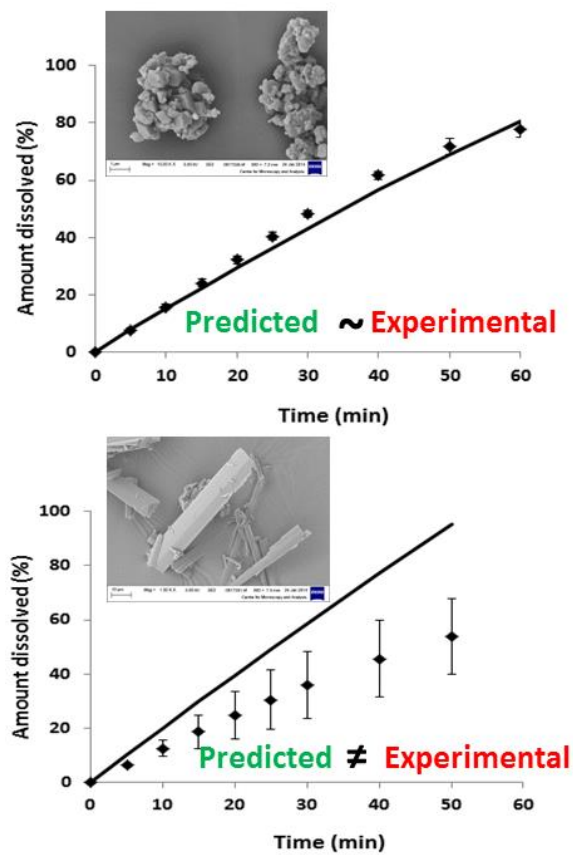
Methods: Cocrystals were produced via milling or solvent mediated processes. *In vitro* dissolution was carried out in the flow-through apparatus, with shadowgraph imaging and mechanistic mathematical models used to observe and simulate particle dissolution. *In vitro* activity was tested using agar diffusion assays.

Results: Cocrystallisation via milling produced small polyhedral crystals with antimicrobial activity significantly higher than sulfadimidine alone, consistent with a fast dissolution rate which was matched only by cocrystals which were milled following solvent evaporation. Cocrystallisation by solvent evaporation (ethanol, acetone) or spray drying produced flattened, plate-like or quasi-spherical cocrystals, respectively, with more hydrophobic surfaces and greater tendency to form aggregates in aqueous media, limiting both the dissolution rate and *in vitro* activity. Deviation from predicted dissolution profiles was attributable to aggregation behaviour, supported by observations from shadowgraph imaging.

Conclusions: Aggregation behaviour during dissolution of cocrystals with different habits affected the dissolution rate, consistent with *in vitro* activity. Combining mechanistic models with shadowgraph imaging is a valuable approach for dissolution process analysis.

Keywords

Cocrystal, crystal habit, shadowgraph imaging, particle tracking velocimetry, dissolution simulation, flow-through cell, aggregation.



Abbreviations

4-ASA

4-Aminosalicylic acid

AI

Aggregation index

BFDH morphology

Bravais, Friedel, Donnay and Harker morphology

DVS

Dynamic vapour sorption

FTIR

Fourier-transformed infrared

PI

Polymorph I

PII-HI

Polymorph II- Habit I

PII-HII

Polymorph II- Habit II

PII-HIII

Polymorph II- Habit III

PII-HIV

Polymorph II- Habit IV

PM

Physical mixture

PSD

Particle size distribution

PXRD

Powder X-ray diffraction

RH

Relative humidity

SDM

Sulfadimidine

SEM

Scanning electron microscopy

1. Introduction

The pharmaceutical industry is facing an oncoming crisis due to the huge pressure to address the high attrition rates in drug development (Babu and Nangia, 2011; Serrano Lopez and Lalatsa, 2013). Issues related to pharmacokinetics and bioavailability are still one of the most common causes of attrition in Phase I studies (Waring et al., 2015). For this reason, inexpensive pharmaceutical strategies to enhance drug dissolution are required, as are strategies which enable high quality, affordable pharmaceutical products to be developed. One approach which has been employed is salt formation; however this is only successful when the active pharmaceutical ingredient (API) contains ionisable functional groups in its chemical structure. To overcome this issue, engineering of pharmaceutical cocrystals based on hydrogen bond formation between the API and the coformer can be advantageous, as there is no need to break or create covalent bonds (Blagden et al., 2007; Miroshnyk et al., 2009). In an ideal scenario, the API would be transformed into a crystalline solid that has improved dissolution, which may be even comparable to that obtained with the amorphous drug, but which has greater physical and chemical stability than its amorphous counterpart (Chadha et al., 2012; Qiao et al., 2011; Serrano et al., 2015a).

Sulfadimidine (SDM) is a poorly-soluble anti-infective agent which belongs to the sulfonamide family, APIs which still enjoy relatively widespread use, especially in developing countries, due to their low cost and wide antibacterial activity in spite of increasing antibiotic resistance (Huovinen et al., 1995). Sulfonamides contain multiple hydrogen bond acceptor and donor functional groups that allow cocrystal formation due to multiple supramolecular interactions (Caira, 1992, 2007). Cocrystallisation of SDM with suitable coformers may favourably alter its biopharmaceutical properties, such as dissolution, and ideally also its activity. Two different polymorphic forms of the cocrystal composed of SDM and 4-aminosalicylic acid (4-ASA) in a 1:1 molar ratio have been reported to improve drug dissolution (Caira, 1992; Grossjohann et

al., 2015). However, the combination of the effects of alterations in both polymorphic form and crystal habit on biopharmaceutical properties still remains poorly understood.

The hypothesis underpinning this work is that engineering SDM into a cocrystal with a cofomer such as 4-aminosalicylic acid (4-ASA), which is proven to possess anti-inflammatory properties (Lover, 1987), could be used as an approach to exploit a synergistic activity between the two compounds. Cocrystal engineering may also induce changes in the crystal habit which could drastically affect the physicochemical properties of the drug and hence its dissolution performance.

Bearing in mind that the dissolution rate of a particle is a function of the local fluid velocity relative to that particle, a combination of factors such as shape and particle size, the density of the particle and the fluid, the absolute fluid velocity and viscosity can affect the process (Sugano, 2008). Generally, dissolution studies focus on the quantification of the drug dissolved with time. However, dissolution is a continuous process and changes in shape and particle size over time will potentially affect the overall dissolution profile. Assessing both drug dissolved and particle size with time should give a deeper understanding of the influence of the physicochemical characteristics of the drug on dissolution and should also facilitate the prediction of *in vivo* performance.

There are several methods to monitor real-time changes in particle size during dissolution, for example laser-based focussed beam reflective measurement, that requires placement of a probe in the vessel of the paddle dissolution apparatus (Han et al., 2009; Zidan et al., 2010). However, this becomes complex when dissolution studies are performed in the flow-through cell apparatus. In order to overcome this issue, shadowgraph imaging can be suitable. This is a relatively inexpensive laser-based optical technique based on a diffuse backward illuminated setup in order to register the shadow image of focused particles on a camera (Legrand et al.,

2014). One of the advantages is that no probe is required; instead an external source and a recording plane (i.e. a camera), onto which the shadow of the varying density field is projected, are necessary (D'Arcy D and Persoons, 2011). A shadow is generated because a laser ray is refractively deflected so that the position on the recording plane where the undeflected ray would arrive remains dark and at the same time the position where the deflected ray arrives appears brighter. A visible pattern of variations of the illumination is produced in the recording plane (Panigrahi and Muralidhar, 2012; Wolfgang, 2011).

In the current work, the aim was to investigate the use of shadowgraph imaging in the flow-through cell dissolution apparatus to determine changes in particle size distribution over the dissolution time course and to use that data to interpret experimental dissolution data, in particular deviations of observed dissolution profiles from simulated profiles. Furthermore we sought to measure and compare the *in vitro* antimicrobial activity of SDM:4-ASA cocrystals with different polymorphic forms, crystal habits and potentially differing dissolution performance characteristics and to relate activity to physicochemical characteristics.

2. Materials and methods

2.1. Materials

SDM and 4-ASA, with a purity $\geq 99\%$, were purchased from Sigma–Aldrich (Wicklow, Ireland). Ethanol and acetone were supplied from Corcoran Chemicals (Dublin, Ireland). HPLC grade methanol was purchased from Fisher Scientific (Dublin, Ireland). Potassium hydrogen phosphate was obtained from Sigma–Aldrich (Wicklow, Ireland) and phosphoric acid from Merck (Darmstadt, Germany).

2.2. Methods

2.2.1. Preparation of polymorphic forms and habits of SDM:4-ASA cocrystal

All cocrystals were prepared using a 1:1 molar ratio (SDM:4-ASA), as previously described (Serrano et al., 2015b).

Briefly, cocrystal Polymorph I (PI) was obtained by liquid-assisted co-milling which was carried out in a planetary ball mill (Retsch PM100, Haan, Germany) as previously described (Grossjohann et al., 2015). Cocrystal Polymorph II- Habit I (PII-HI) was obtained by crystallization from ethanol using a rotavapor (Buchi, Flawil, Switzerland) at 250 mbar pressure and 55 °C as previously described (Serrano et al., 2015b). Cocrystal Polymorph II- Habit II (PII-HII) was obtained by crystallization from acetone also using a rotavapor (Buchi, Flawil, Switzerland) at 250 mbar pressure and 55 °C as previously described (Serrano et al., 2015b). Cocrystal Polymorph II- Habit III (PII-HIII) was obtained by spray-drying ethanolic solutions of SDM:4-ASA (1:1 molar ratio) using a Buchi B-290 Mini Spray Dryer (Buchi, Flawil, Switzerland) operating in the open-mode, as previously described [12]. Cocrystal Polymorph II- Habit IV (PII-HIV) was obtained from polymorph II- Habit I after dry milling in a planetary ball mill (Retsch PM100, Haan, Germany) as previously described (Serrano et al., 2015b). An equimolar physical mixture (PM) of 4-ASA and SDM was prepared by mixing the raw components in a mortar and pestle.

2.2.2. Physicochemical characterisation

Powder X-ray diffraction (PXRD)

Powder X-ray analysis was performed using a Rigaku MiniflexII desktop X-ray diffractometer (Rigaku, Tokyo, Japan) with Haskris cooling unit (Grove Village, IL, USA) as previously described [21]. The PXRD patterns were recorded (n=3) from 5° to 40° on the 2 theta at a step scan rate of 0.05° per second (Paluch et al., 2013a).

Fourier-transformed infrared Spectroscopy

IR spectra were recorded on a PerkinElmer Spectrum 1 FTIR Spectrometer (PerkinElmer, Massachusetts, USA) equipped with a UATR and a diamond/ZnSe crystal accessory as previously described [12]. Baseline correction and data normalization were performed using Spekwin32 version 1.71.6.1.

Particle size distribution analysis (PSD)

The geometric particle size distributions (PSD) were determined by laser diffraction using a Malvern Mastersizer 2000 (Malvern Instruments Ltd., Worcestershire, U.K.). Particles were dispersed using a Scirocco dry feeder instrument with 1 bar pressure. An obscuration of 1–6% was obtained under a vibration feed rate of 50%. Liquid measurements in deionised water were carried out using a Hydro 2000 μ P accessory (for small volume wet sample dispersions). Samples were analysed based on the D_{10} , D_{50} , D_{90} in two different ways: i) as diluted suspensions and ii) as concentrated suspensions similar to the conditions in the flow-through cell of the dissolution apparatus. Diluted suspensions were prepared by dispersing the powder (2 mg) in deionised water (2 ml) before adding it into the cell (18 ml) and performing the measurement at 2000 rpm and 50% output ultrasounds to avoid aggregation. Concentrated systems were generated by adding 50 mg of powder directly into the cell and keeping a constant stirring rate of 1000 rpm initially without ultrasounds. Measurements were performed at different time points (0, 1, 2, 3, 4, 5, 6, 7, 8, 9, 10, 15, 20, 25 and 30 min). Subsequently, three ultrasound cycles (1 min each at 80% power) were applied. Particle size was measured after each cycle. Aggregation indices (AI) were determined based on four ratios: AI_1 , AI_2 , AI_3 and AI_4 which were calculated as shown in the Equations 1, 2, 3 and 4.

$$AI_1 = \frac{D_{50}(t_{30})}{D_{50}(t_0)} \quad \text{Equation 1}$$

$$AI_2 = \frac{D_{90}(t_{30})}{D_{10}(t_{30})} \quad \text{Equation 2}$$

$$AI_3 = \frac{D_{50}(t_{30+US})}{D_{50}(t_{30})} \quad \text{Equation 3}$$

$$AI_4 = \frac{D_{50}(liquid)}{D_{50}(solid)} \quad \text{Equation 4}$$

Where $D_{50}(t_0)$ is the median particle size measured immediately after the powder was added to the cell under a constant stirring rate of 1000 rpm, $D_{50}(t_{30})$ is the median particle size 30 min after the powder was added on the cell under a constant stirring rate of 1000 rpm, $D_{90}(t_{30})$ represents the diameter for which ninety percent of the distribution has a smaller particle size than that diameter 30 min after the powder was added to the cell under a constant stirring rate of 1000 rpm, $D_{10}(t_{30})$ represents the diameter for which ten percent of the distribution has a smaller particle size than that diameter 30 min after the powder was added on the cell under a constant stirring rate of 1000 rpm, $D_{50}(t_{30+US})$ is the median particle size 30 min after the powder was added on the cell and after one cycle of ultrasound at 80% power under a constant stirring rate of 1000 rpm, $D_{50}(liquid)$ is the median particle size of the diluted suspension and $D_{50}(solid)$ is the median particle size of the solid powder. Results reported are the average of three analyses.

True density measurements

The true density was measured by an Accupyc 1330 Pycnometer (Micromeritics, Norcross, GA, USA) using helium (99.995% purity) to determine the volume of the sample as previously described (Paluch et al., 2013b). Samples were dried under N_2 atmosphere prior to measurement for 24 h at 25 °C. Results are the average of three analyses.

Scanning electron microscopy (SEM)

Surface images of powders were performed by SEM using a Zeiss Supra Variable Pressure Field Emission Scanning Electron Microscope (Supra Series, Oberkochen, Germany) equipped with a secondary electron detector at 5 kV. Samples were glued onto aluminium stubs and sputter-coated with gold under vacuum prior to analysis (Mugheirbi et al., 2014).

Dynamic vapour sorption (DVS)

Sorption isotherms and kinetic profiles of the formulations were obtained using a DVS (Advantage, Surface Measurement Systems, Alperton, UK) at $25.0 \pm 0.1^\circ\text{C}$. Water was used as the probe vapour. Samples were dried at 0% RH for 1 h and then subjected to step changes of 10% RH up to 90% RH, and the reverse for desorption. The sample mass was allowed to reach equilibrium, defined as $dm/dt \leq 0.002$ mg/min over 10 min, before the RH was changed (Curtin et al., 2013). Sample weights were between 10 and 15 mg. The crystalline nature of the systems after DVS analysis was confirmed by PXRD.

2.2.3. Flow-through cell dissolution studies and HPLC analysis

A single flow-through cell dissolution apparatus (Sotax AG, Basel, Switzerland) in an open-loop configuration with an internal diameter of 12 mm was used. The amount of powder loaded in every study was 300 mg. A cellulose Whatman[®] filter grade 1 (11 μm), a glass microfiber filter (Whatman[®] GF/D, 2.7 μm), a glass microfiber Whatman[®] filter grade GF/F (0.7 μm) and a hydrophilic membrane Pall Supor[®] (0.45 μm) were positioned sequentially at the inner top of the cell to retain undissolved material. The dissolution test was operated at $37 \pm 0.5^\circ\text{C}$ with a flow rate of 8 ml/min over 60 min using deionised water without any surfactant. Dissolution studies for PM, PI and PII-HI were also performed using two different buffers (pH 1.2 from 0 to 60 min and pH 6.8 from 60 to 180 min) prepared as described in the US Pharmacopeia (USP, 2008). Buffer at pH 1.2 was prepared by mixing 250 ml of NaCl (0.2 M) and 425 ml of HCl

(0.2 M), made up to a final volume of 1000 ml with deionised water. Buffer at pH 6.8 was prepared by mixing 250 ml of KH_2PO_4 (0.2 M) and 112 ml of NaOH (0.2 M) made up to a final volume of 1000 ml with deionised water. The temperature was maintained at $37 \pm 0.5^\circ\text{C}$ during testing. Samples were collected from the flow-through cell at different time points, diluted with mobile phase and analysed by HPLC to calculate the percentage of drug dissolved at each time point. Briefly, the mobile phase consisted of methanol/buffer pH 6.5 40/60 (v/v). The buffer was prepared from a 50 mM dipotassium phosphate solution adjusted to pH 6.5 with phosphoric acid. HPLC analysis was performed using an Alliance HPLC with a Waters 2695 Separations module system and Waters 2996 Photodiode array detector. Separation was performed on a Phenomenex Inertsil ODS (3) C18 column (150 mm length, diameter 4.6 mm, particle size 5 μm) at a UV detection wavelength of 265 nm with an injection volume of 20 μL . The elution was carried out isocratically at ambient temperature with a flow rate of 1 ml/min. In a different experiment, samples were collected from the inside the cell of the flow through apparatus at different time points, dried at ambient temperature under a nitrogen atmosphere and analysed by PXRD to assess in situ-solid state transformations.

2.2.4. Shadowgraph imaging and particle tracking analysis

Shadowgraph imaging studies were carried out on the single cell of a CE-1 flow-through dissolution apparatus (Sotax AG, Basel, Switzerland) loaded with 50 mg of powder and using deionised water as medium. The flow rate was 8 ml/min. In order to monitor the particle size distribution over time, the following was used: i) a double-frame camera (Photron Fastcam SA1, Photron UK, West Wycombe, Bucks., UK), 1024 \times 1024 pixel, 12 bit) with high magnification lens that captures digital images of the particle-laden fluid against a uniform pulsed background illumination and ii) a Nikon 105-mm lens mounted on a 150-mm long extension tube, resulting in a field of view of 6 \times 6 mm (i.e. resolution= 6 μm per pixel; magnification = 3.33:1) of the bottom right-hand side of the dissolution cell to ensure sufficient

pixel resolution of the smallest particles for the given camera sensor. (The Setup for shadowgraph imaging is shown in Figure S1 in supplementary material). (D'Arcy D and Persoons, 2011). The measurement volume thickness was defined by the focal plane and depth of focus of the imaging system, which was about 1 mm and intersected the centreline of the test cell. On the basis of a pair of images acquired 100 milliseconds apart, individual particle velocities were determined. Bias contributions of defocused particles outside the measurement volume were minimised by an appropriate choice of detection thresholds. Images were acquired using LaVision DaVis 7.2.2 software (LaVision GmbH, Göttingen, Germany) and particle sizes and velocities were determined using a code developed in-house, and implemented in Matlab (The MathWorks, Natick Massachusetts, USA) (D'Arcy D and Persoons, 2011).

2.2.5. Mechanistic mathematical model

The dissolution simulation model was previously described by D'Arcy et al. (D'Arcy D and Persoons, 2011) and uses Matlab (The MathWorks, Natick Massachusetts, USA) to solve the equations. The dissolution system was simplified to a zero dimensional model (D'Arcy D and Persoons, 2011) describing the evolution of particle velocity and diameter during dissolution in the oscillating flow dissolution test cell. The inputs for the model were the initial median particle size in the liquid media, the oscillating fluid velocity enforced by the pump (8 ml/min), fluid density (0.993 g/cm^3), fluid dynamic viscosity ($7 \times 10^{-4} \text{ Pa s}$), diffusion coefficient for SDM in free water ($5 \times 10^{-10} \text{ m}^2/\text{s}$) (Larsbo et al., 2008) and the material properties such as: true density, equilibrium solubility in deionised water at $37 \text{ }^\circ\text{C}$ (2.5×10^{-3} and 2.75×10^{-3} mmol/ml for polymorph I and II respectively (Grossjohann et al., 2015). The main assumptions of the model are that (i) the particles are rigid and spherical in shape; (ii) there is no interaction between particles; (iii) the velocity field in the test cell is uniform and unidirectional.

2.2.6. Molecular modelling

The program Mercury (version 3.5.1., Cambridge Crystallographic Data Centre, Cambridge, UK) was used to calculate X-ray powder patterns on the basis of the single crystal structure and to identify Miller's indices of various facets of the crystal. Mercury[®] was also used to predict the Bravais, Friedel, Donnay and Harker (BFDH) morphology and full interaction map to get an insight into the molecular arrangement on different crystal facets of the cocrystal.

2.2.7. *In vitro* antimicrobial activity

The *in vitro* activity of the different cocrystals was evaluated against *Staphylococcus aureus* (CECT 239) *Staphylococcus Epidermis* (CECT 231) and *Bacillus subtilis* (CECT 356) as examples of Gram-positive bacteria, and *Pseudomonas aeruginosa* (CECT 108) and *Escherichia coli* (CECT 515) as examples of Gram-negative bacteria (Darwish et al., 2014). All the strains were obtained from the Colección Española de Cepas tipo. They were also evaluated for *in vitro* antiprotozoal activity against different *Leishmania* spp. (*L. infantum*, *L. donovani* and *L. amazonensis*) (Ruiz et al., 2014).

The antibacterial activity assays were carried out using the agar diffusion assay according to the USP Pharmacopoeia (2008) (USP, 2008). The antibacterial activity assays were tested using Mueller-Hinton agar plates inoculated with a suspension (equivalent to a 0.5 McFarland standard) of the clinical isolates. Each sample (50 mg) was diluted in deionised water to a final concentration of 500 µg/ml. Aliquots of this initial suspension were further diluted to obtain the following concentrations of SDM: 500, 250, 125, 62.5, 31.25, 15.6 µg/mL. The *in vitro* activity of 4-ASA at the same concentrations was also assessed. Paper disks were embedded with 20 µl of each sample. Once the disks were dried, they were placed onto the inoculated agar plates. The plates were incubated at 35 °C for 24 hours and the growth inhibition zone diameters (mm) were carefully measured with a callipers (Darwish et al., 2014). All tests were carried out in triplicate.

Antiprotozoal in vitro activity was tested against promastigotes of *L. infantum* (MCAN/ES/96/BCN150), *L. amazonensis* (MHOH/BR/79/MARIA) and *L. donovani* (MHOM/IN/80/DD8 ATCC ® 50212™). The assays were carried out as previously described (Dea-Ayuela et al., 2009; Sobarzo-Sanchez et al., 2013). Different dilutions of the samples were tested between 3.125 and 200 µg/ml. All tests were carried out in triplicate.

2.2.8. Statistical analysis

Statistical analysis was performed via one-way ANOVA Test using Minitab 16 (Minitab Ltd, Coventry, UK) followed by Tukey's test considering p-values < 0.05 for statistical significance.

3. Results and discussion

3.1. Characterisation and molecular modelling of SDM:4-ASA polymorphic cocrystals and crystal habits

PI was successfully produced by liquid-assisted milling while PII was obtained after crystallisation from different solvents (ethanol or acetone) or by spray-drying. The different manufacturing processes led to a variety of crystal habits as shown by SEM micrographs: clusters constituted of small polyhedral crystals for PI, flattened-large crystals for PII-II, large plate-like crystals for PII-III, microspheres for PII-III and clusters constituted of small cube-like crystals for PII-IV. The crystal habit of the PM was a mixture of the crystal habits of the single components: elongated rectangular crystals for 4-ASA and plate-like crystals for SDM (Table 1). PXRD analysis showed that the diffractograms of both polymorphic cocrystals of 4-ASA and SDM exhibited patterns with characteristic diffraction peaks which differ between one another and also differ from those of the single components as previously described (Figure 1). Bragg peak positions of polymorph II were the same in all the crystal habits (I to IV) but,

the peak intensity varied, indicating different preferred orientation of the crystallographic planes (Figure 1).

Results of IR spectroscopy are illustrated in Figure 2. Similar to PXRD analysis, distinctive bands for both polymorphic cocrystals of 4-ASA and SDM were observed showing shifts to different wavenumbers with respect to the single components and between each polymorph. However, no shifts were observed between the different crystal habits of PII, which showed characteristic bands at 3469, 3416, 3368, 3341 and 3488, 3394 and 3375 cm^{-1} respectively. These bands can be attributed to the asymmetric and symmetric N-H stretching vibrations of the amine group and O-H stretching (H-bonded) bands which are shifted to different wavenumbers compared to SDM (3442, 3341 and 3240 cm^{-1}) and 4-ASA (3496 and 3387 cm^{-1}). Differences between PI and PII were observed in the bands corresponding to the sulfone group at 1301 and 1318 cm^{-1} respectively (attributed to asymmetric S=O stretch vibrations), at 1144 and 1149 cm^{-1} respectively (attributed to symmetric S=O stretch vibrations) and at 884 cm^{-1} (attributed to the S-O stretch) which was only observed in the PI. Other characteristic bands related to C-N stretch and C-O stretch (for the carboxylic acid group) vibrations were found at 1270 and 1094 cm^{-1} for PI and at 1282 and 1084 cm^{-1} for PII respectively.

As observed in Figure 3a-c, the main functional groups involved in the cocrystal formation by means of H-bonds are the sulfone and the amine groups from the SDM and the carboxylic acid and alcohol groups from the 4-ASA. The shifts in IR bands detailed above provide clear evidence of hydrogen bonding interactions between these functional groups. The difference in shifted bands between PI and PII can be explained by the different arrangement of the atoms in the crystal lattice of each polymorph (Figure 3).

Mercury[®] 3.5 software was used to identify the Miller's indices of various facets of the crystal and also to predict the BFDH morphology and full interaction map to get an insight into the

possible interactions of the cocrystals with the environment through hydrophobic interactions such as π - π stacking and hydrogen bond formation (both donor and acceptor). The results are shown in figure 3. Miller's indices (hkl) corresponding to various facets of the crystal are represented in Figure 1. The positions of the Bragg peaks were in agreement with the simulated powder patterns for the crystal structure available in the Cambridge Structural Database (CSD) (Refcode: VUGMOZ P-1 and P212121).

The BFDH simulation of crystal morphology and the full map interaction (Figure 3d,e) showed that the facet (010) has hydrophobic groups (-CH₃) exposed whereas the facets (1-10), (10-1), (100), (1-11) and (01-1) have hydrophilic groups exposed with the potential to form H-bonding, necessary to facilitate wetting of the powder and hence dissolution. The growth of the PI cocrystal in vacuum (as predicted by the BFDH method) is dominated by the (01-1) and (20-2) facets and to a lesser extent by the (020) facet (Figure 1). In the process of ball milling, PI preferentially fractured along one of its shortest axes (Ho et al., 2012), exposing (20-2) plane (parallel to the facet (10-1)) with increased cube aspect ratio and hydrophilicity resulting in higher surface capacity for interaction by H-bonding, whereas the plane (020) which is expected to be parallel to the hydrophobic facet (010) is less exposed after the milling process (See supplementary material, Figure S2).

The BFDH morphology and map interaction for PII showed that the most hydrophobic facets were (200), (-110), (01-1), (011) and (110) whereas the highest hydrophilic surfaces were found on the (-10-1) and (10-1) facets due to -NH₂ and sulfone groups. The most important facet exhibited by PII-HI was (011) but it also showed a prominent (101) facet as indicated by PXRD data (Figure 1). Other facets such as (110) and (400), parallel to (200), grew less compared to other cocrystal habits. PII-HII showed characteristic prominent hydrophobic facets characterized by faster growth of the (400) and (411) facets along with the (011) facet.

However, in PII-HIII and PII-HIV the (011) and (110) facets were responsible for the largest facet surfaces.

Application of the BFDH theory is a fast tool for identifying the crystallographic forms that are most likely to constitute a crystal habit. According to this theory, the relative growth rate of a face is inversely proportional to the interplanar spacing, d , and hence those facets with the biggest d values will be the most morphologically important facets of the crystal (Donnay and Harker, 1937; Mirza et al., 2009). The comparison of the predicted BFDH habit with the observed morphology of the cocrystals indicates that the morphology of the PI cocrystal is in reasonable agreement with the BFDH model. However, predictions are not as accurate for PII. One of the reasons is that PII was obtained after crystallization from different solvents and the BFDH predicts the morphology based on the internal structure in vacuum without taking into account chemical bonding or the energetics of the system such as API-solvent interactions (Chen et al., 2013). Thus, the stronger the bonding effects in the crystal, the less accurate the model becomes. Nevertheless, overall PI exhibited a higher surface density of H-donor regions compared to PII which showed more prominent hydrophobic domains.

3.2. DVS isotherms and water uptake

The DVS isotherms for PI, PII and PM are illustrated in Figure 4. Despite significant differences in the sorption profiles between the cocrystals, all of them can be classified as slightly hygroscopic according to the hygroscopicity classification system (criteria: essentially no moisture increase below 80% RH with an increase in mass $< 2\%$ but $\geq 0.2\%$) (Murikipudi et al., 2013). The maximum water sorption for the PM was below 2% showing a rapid uptake of water at higher relative humidities (Figure 4a). The subsequent water desorption due to decreasing humidity occurs more slowly than the sorption process, resulting in hysteresis. This effect is often observed with materials that contain mesopores (internal cavities of 2-50 nm in diameter) where the adsorbed water is condensed. In contrast, the maximum water sorption of

the PI cocrystal polymorph was less than 0.25%. The desorption behaviour was similar with a slight hysteresis effect in the humidity range of 90-40% RH, followed by merging with the sorption profile below 40% RH (Figure 4a).

The water sorption profile varied among the cocrystal habits of PII. PII-HI and HII showed a similar profile to PI, characterised by a low water uptake over the entire humidity range, whereas PII-HIII showed a relatively strong increase in water sorption between 80 and 90% RH (Figure 4b). The desorption behaviour of PII-HIII was associated with a hysteresis effect in the humidity range of 90-40% followed by merging with the sorption profile below 40%. PII-HIV showed a maximum water sorption less than 0.6%. Similarly, the desorption behaviour was associated with a hysteresis effect over the entire humidity range (Figure 4a). The DVS isotherm for both PII-HIII & IV is related to their smaller particle size (and hence, higher surface for adsorption) and the partial amorphous state of the systems, leading to a higher water uptake and slower diffusion of water back out of the internal structure (Hassel and Hesse, 2007; Sun, 2011). As shown in Figure 1, both systems exhibited broader Bragg peaks compared to PII-HI & II due to the nature of the production method (spray drying and crystallisation from solution followed by milling). Powder X-ray diffraction analysis of the materials recovered at the end of the experiment revealed no changes compared with the starting materials (data not shown).

3.3. Dissolution modelling and shadowgraph imaging analysis

The modelling of the dissolution of SDM from the equimolar PM was in good agreement with the experimental dissolution profile for the first 10 min, which was characterised by a fast release (Figure 5). However, this rapid drug release was followed by a levelling off in dissolution rate for the remainder of the dissolution time course, which resulted in an overestimation in the simulated dissolution profile. As previously described, the dissolution profile was incongruent, characterised by a larger and faster release of 4-ASA compared to

SDM (Serrano et al., 2015b). Newer findings suggest that the *in situ* formation of the PI cocrystal could lead to a change in the initial release rate of SDM, contributing to the fast release observed up to 10 min. PXRD analysis of the solid contents in the flow-through cell showed that the solid phase in the dissolution medium (water) after 5 min dissolution was a mixture of PI cocrystal and traces of SDM (Figure S3, see supplementary material). Two key factors that determine the accuracy of the dissolution simulation are drug solubility and particle size. Both SDM and PI have similar solubility in aqueous media (Grossjohann, 2013) and also relatively close particle size (D_{50} liquid, Table 1) which explains why modelling of the dissolution of SDM from the PM was in good agreement with the experimental values at earlier times, in spite of PI formation.

Due to the faster release of 4-ASA, SDM is in molar excess over the dissolution time course compared to the coformer, which explains why SDM traces were also found. Along with PI transformation, very large particles were formed during PM dissolution (reflected in the very high AI_1 value) which could be related to a co-precipitation of PI and SDM. To further explore this observation, dissolution studies of PM were also performed at pH 1.2 from 0 to 60 min. Ionisation of SDM ($-NH_3^+$) at this pH plays a key role, leading to greater solubility and consequently faster dissolution rate (Figure S4, see supplementary material). The PM exhibited a two-fold increase in SDM dissolved after 10 min compared to dissolution in deionised water. PXRD analysis again showed *in situ* formation of the PI cocrystal at early time points (5 min), which is presumed to also contribute to the fast release (Figure S5, see supplementary material). However, traces of SDM were observed mainly after 60 min, when the pH of the medium was shifted from 1.2 to 6.8. Therefore the large particles formed during dissolution in deionised water were likely to be co-aggregates of unionised SDM and PI formed *in situ*. No significant differences were observed in dissolution profiles between polymorphs and cocrystal habits at pH 1.2, due to the rapid dissolution rates (Figure S4, supplementary material).

The overall amount dissolved at 60 min was higher for PI and PII-HIV (about 80% release) followed by PII-HI > PII-HII > PII-HIII. Experimental values were in good agreement with the simulated dissolution profile for PI and PII-IV. The faster cocrystal dissolution from PII-IV could be explained by the polymorphic transformation of PII-IV into PI in water during dissolution at very early time points, but also due to the engineered crystal habit as previously reported (Serrano et al., 2015b). The simulations for PII-HI, HII and HIII predicted the same rank-order of dissolution rates as experimental observations, but simulated dissolution rates were faster than experimental in each case. PII-HIII was partially transformed into PI but also free SDM which could explain why the dissolution rate was decreased relative to the other habits of PII. However, polymorphic transformations alone cannot explain differences between the dissolution rates of the different PII crystal habits and the influence of particle aggregation should also be borne in mind. For this reason, shadowgraph imaging studies were performed in an attempt to gain insight into the particle behaviour in the flow-through cell apparatus (Figure 6 and Figure S6 in supplementary material).

The laser-based background illumination source was aligned with one of the lower corners of the cell, above and to one side of where the sample was initially located. It is worth noting that only particles within the measurement region contribute to the results of the sizing analysis discussed below. PI and PII-HIV showed a similar shadowgraph imaging pattern which explains their higher dissolution rates relative to the other cocrystal forms. At time zero, a unimodal particle size distribution ranging from about 30 to 250 μm in diameter was observed. At the 500 s dissolution time point, the number of particles with larger size was diminished, resulting in an increase in the smaller subgroups of 40 and 20 μm . At 1000 s, the particle size profile was similar to the one at 500 s with a reduced number of particles above 100 μm indicative of no further aggregation occurring over time. Therefore, the particle size

distribution of PI and PII-HIV was indicative of deaggregation/dissolution of bigger clusters leading to the appearance of smaller particles in suspension.

Shadowgraph imaging studies of PII-HI, PII-HII and PII-HIII showed a similar pattern characterised by a slower deaggregation and dissolution of big clusters into smaller particles and the persistence of a population of larger particles ($> 100 \mu\text{m}$). This could explain why the predicted amounts dissolved were greater than the experimental ones in these systems. Although PII-HI showed large aggregates at earlier time points, over time, the number of smaller particles ($< 20 \mu\text{m}$) was increased compared to PII-HII and PII-HIII. The existence of big clusters was noticeable for PII-HII and PII-HIII. After 1000 s, two particle size populations ($< 100 \mu\text{m}$ and $> 100 \mu\text{m}$) with similar number of particles each were clearly observed. The aggregation tendency could be interpreted as aggregation of particles suspended in the dissolution media but also could suggest the tendency of formation of a powder bed (Figure S6). The particles in a powder bed would be exposed to different flows and local concentrations to those suspended in the dissolution media. One of the reasons that could explain why PII-HI has a lower tendency to form aggregates in aqueous medium compared to PII-HII and PII-HIII could be the crystallographic planes and facets exposed to the liquid medium. As previously commented, PII-HI exhibits more prominently hydrophilic facets and less hydrophobic facets such as (101) and (110) and (400) respectively.

With the aim of supporting the conclusions drawn from the shadowgraph imaging studies, PSD of concentrated systems imitating the conditions in the flow-through cell at earlier time points was studied (Table 1).

Four aggregation indices were calculated in order to understand the behaviour of the systems under different circumstances. The first aggregation index (AI_1) evaluated the tendency to form aggregates over time (after 30 min) under mild stirring conditions. The PM exhibited the

highest AI_1 value (21.7) followed by PII-HIII > PII-HII > PII-HI \approx PI-HIV \approx PI. These results confirm the aggregation tendency observed in PII-HIII and PII-HII and the deaggregation of big clusters over time in PI and PII-HIV (Figure S7, see supplementary material).

The second aggregation index (AI_2) evaluated the polydispersity in particle size over time. The higher the difference between the D_{90} and the D_{10} at 30 min, the higher the AI_2 . PII-HI, PII-HII and PII-HIII exhibited a higher AI_2 compared to PI and PII-HIV. Both PI and PII-HIV showed a shift in particle size from larger to smaller bimodal distributions predominantly constituted by subpopulations of <20 and from 20 to 70 μm . However, in the other three systems (PII-HI, PII-HII PII-HIII) bigger aggregates remained present over time, which makes the difference between the D_{90} and D_{10} larger. In contrast, the PM exhibited the smallest AI_2 . Initially, the particle size distribution of the PM showed a bimodal distribution that corresponds to the particle size of the single components ($D_{50} = 34 \mu\text{m}$ for SDM and $D_{50} = 339 \mu\text{m}$ for 4-ASA). Over time, the particle size shifted to much larger aggregates, therefore the volume of smaller particles in suspension was reduced. This can explain the low value for AI_2 and also why the dissolution profile levelled off after 20 min.

The third aggregation index (AI_3) evaluated the effect of ultrasonic cycles in PSD. It can be assumed that a short ultrasonic cycle should break up the larger aggregates, resulting in smaller particles in suspension unless the H-bonding, electrostatic and hydrophobic forces between particles are so strong that ultrasounds lead to further particle interaction resulting in aggregation. PSD was reduced after one ultrasonic cycle in the PI, PII-HI and PII-HIV leading to an $AI_3 < 1$. In contrast, particle size was not altered or slightly increased ($AI_3 \geq 1$) in the other systems, which was related to stronger interactions between the hydrophobic crystal facets.

The fourth aggregation index (AI_4) showed the increase in particle size when powder is dispersed in aqueous media. The higher the AI_4 , the larger the increase in PSD in deionised water. PII-HIII exhibited the highest value of AI_4 , which supports the slow dissolution rate in spite of it being the system with the smallest particle size in the solid state. The fact that PII-HII exhibits more prominently hydrophobic facets (110) and (101) than the other polymorph or PII crystal habits is thought to contribute to the increased tendency of PII-HII to aggregate, in an attempt to protect hydrophobic facets from the aqueous environment. In contrast, PI displayed the lowest AI_4 and the least tendency to aggregate in aqueous media.

Off-line measurement of PSD through laser diffraction as used in the current study offers the advantage of being able to investigate aggregation tendencies under a range of controlled conditions. However, it is worth noting that particle size is measured in a closed system (which could promote increased aggregation behaviour compared to within the flow-through cell, using the open loop configuration). In contrast, the shadowgraph imaging studies provide real time observations on particle size behaviour during dissolution, but without similar scope to control the particle environment. Therefore combining information on observed aggregation tendencies from the calculated aggregation indices, with online observations from dissolution shadowgraph imaging, offers an approach for exploring the interplay between particle size, aggregation and dissolution behaviour.

Comparisons between experimental and simulated dissolution profiles were made for deionised water, because differences in dissolution rates between polymorphs and cocrystal habits were clearly observed, while no significant differences were found at pH 1.2 due to much faster dissolution profiles (Figure S4, see supplementary material). The dissolution simulation model incorporates the particle size in liquid, capturing initial aggregation; however it does not capture particle aggregation over time, flow within the powder bed, nor any density variation due to aggregation of particles (which would also affect relative velocity). The aggregation

behaviour of PII-HI, PII-HII and PII-HIII therefore supports the lower observed dissolution rates in contrast to the simulated dissolution rates in each case. Furthermore, in terms of the PM, the large co-aggregates formed over the course of the dissolution explain the levelling of the observed SDM dissolution profile in contrast to the simulated profile. The lack of aggregation behaviour of PI and PII-HIV, along with the close match of simulated to observed results for these co-crystal forms, suggest that aggregation behaviour of cocrystals is an important property for accurate quantitative simulation of their dissolution behaviour, though a qualitative rank order prediction was possible without this information. Similarly, deviation of observed cocrystal dissolution profiles from simulated profiles would suggest that aggregation behaviour should be investigated.

3.4. *In vitro* activity

Cocrystals and SDM exhibited *in vitro* antimicrobial activity against the Gram-positive bacteria *S.aureus* and *B. subtilis* (Figure 7) whereas they did not show activity against Gram-negative bacteria or *Leishmania* parasites at the concentrations tested. The coformer (4-ASA) also showed antibacterial activity but only at higher concentrations ($> 250 \mu\text{g/ml}$). No significant differences were observed between the PM and SDM. PI, PII-HI and PII-HIV showed a 2.8, 2.3 and 1.8-fold higher ($p < 0.05$) *in vitro* activity than SDM against *S. aureus* at low concentrations ($31.25 \mu\text{g/ml}$). PI was the only system that was still active at $15.63 \mu\text{g/ml}$. PII-HII and PII-HIII showed poorer activity against *S. aureus* than PI and PII-HI.

However, both polymorphic cocrystals and all the crystal habits also showed significantly higher activity than SDM at $31.25 \mu\text{g/ml}$ against *B. subtilis*. In addition, PI, PII-HI and PII-HIV also exhibited higher activity (1.94, 2.05 and 2.0-fold respectively) than SDM at higher concentrations ($62.5 \mu\text{g/ml}$).

Dissolution performance plays a key role in the *in vitro* antibacterial activity of the systems. SDM acts by inhibiting bacterial synthesis of dihydrofolic acid by means of competing with para-aminobenzoic acid for binding to dihydropteroate synthetase. If the system aggregates in aqueous media (as all the systems were present in suspension rather than in solution for all the concentrations tested), dissolution is retarded and there is less available dissolved SDM to interact with the bacteria and exert its activity. Although 4-ASA also has activity against both bacteria strains, the PM did not lead to a synergistic effect probably due to its dramatic tendency to form aggregates in an aqueous medium. A similar effect was also observed with PII-HII and PII-HIII which also translated into a low *in vitro* efficacy. In contrast, the systems with the fastest dissolution rate (PI, PII-HI and PII-HIV) exhibited the highest *in vitro* activity.

4. Conclusions

Crystal habits can have a great influence on the physicochemical and biological properties of the drug. Even for cocrystals with poor pharmaceutical properties, when a suitable coformer and manufacturing process is selected, a habit may be engineered which leads to a better dissolution profile and *in vitro* activity. Despite the fact that PII has a higher aqueous solubility compared to PI, the crystal habit plays a key role in the overall dissolution profile as a consequence of the facets that are predominantly exposed to the dissolution media, that determine the propensity for the formation of either H-bonds or hydrophobic interactions with the environment. Mechanistic mathematical models are useful, not only as a quick approach to predict the dissolution profile of the cocrystals, but also to identify situations where the dissolution process deviates from that expected/predicted. A deeper understanding of the dissolution performance is therefore critical, such as monitoring not only the amount of drug dissolved but also changes in particle size over the dissolution time course. Inexpensive laser-based optical techniques like shadowgraph imaging have shown to have a great potential as they allow real-time measurements of particle size. Cocrystallisation via milling (PI and PII-

HIV) of SDM with 4-ASA led to a 2.3-fold higher drug release at 60 min compared to other polymorph habits, and significantly higher antibacterial activity due to a synergistic effect between drug and conformer, whereas cocrystallisation by solvent evaporation or spray drying led to SDM:4-ASA cocrystals with a more hydrophobic surfaces and tendency to form aggregates in aqueous media, limiting both its dissolution rate and *in vitro* activity.

Acknowledgements

This publication has emanated from research conducted with the financial support of Science Foundation Ireland under Grant Number SFI/12/RC/2275.

Legend to Figures

Figure 1. PXRD patterns of different polymorphs and habits of SDM: 4-ASA (1:1 molar ratio) cocrystal and starting materials (modified from (Serrano et al., 2015b)). Miller's indices of various facets of the crystal were identified by using Mercury[®].

Figure 2. FTIR spectra of different polymorphs and habits of SDM: 4-ASA (1:1 molar ratio) cocrystal and starting materials.

Figure 3. Visualization of molecular surface and molecular interactions using Mercury[®] 3.5.1. software. Key: a) Chemical structure of 4-ASA; b) Chemical structure of SDM; c) Hydrogen bonding interactions between SDM and 4-ASA in the polymorph I; d) Predicted BFDH crystal morphology of polymorph I; e) Predicted BFDH combined with full interaction map showing the functional groups involved in the H-bond and hydrophobic interactions of the cocrystal polymorph I with its surroundings; f) Predicted BFDH crystal morphology of polymorph II; g) Predicted BFDH combined with full interaction map showing the functional groups involved in the H-bond and hydrophobic interactions of the cocrystal polymorph II with

its surroundings. Blue colour represents – H-bond donor, red colour represents- H-bond acceptor and orange colour represents– hydrophobic interaction.

Figure 4. Stability studies. Moisture sorption (solid line) and desorption (dashed line) profiles of SD:4-ASA 1:1 form I and form II cocrystal at 25°C. Key: a) PM (—▲—); PI (—●—); PII-HIV (—■—); b) PII-HI (— - —); PII-HII (—◆—) and PII-HIII (—x—).

Figure 5. Experimentally determined and simulated (solid line) dissolution profiles of 300 mg of sample in the flow-through cell at 8 ml min⁻¹ in deionised water.

Figure 6. Number of particles at each particle size range as determined by the shadowgraph imaging method, along with corresponding particle velocity (cm s⁻¹) at 0, 500 and 1000 s approximately. Data taken from 50 mg of sample in deionised water at 8 ml/min. Left to right: Data for different polymorphs/habits as indicated. Top to bottom: Measurement results averaged over 5 seconds at approximately $t = 0, 500, 1000$ seconds of dissolution.

Figure 7. *In vitro* antibacterial activity. The *in vitro* activity both polymorphs and crystal habits were tested against *S. aureus* and *B. subtilis* and compared to the single components and the PM. Each sample was diluted in deionised water and tested at the following concentrations of SDM: 500, 250, 125, 62.5, 31.25, 15.6 µg/mL. The *in vitro* activity of 4-ASA at the same concentrations was also assessed. Statistically significant differences: * = $p < 0.05$ versus SDM.

References

- Babu, N.J., Nangia, A., 2011. Solubility advantage of amorphous drugs and pharmaceutical cocrystals. *Cryst. Growth Des.* 11, 2662-2679.
- Blagden, N., de Matas, M., Gavan, P.T., York, P., 2007. Crystal engineering of active pharmaceutical ingredients to improve solubility and dissolution rates. *Adv. Drug Deliv. Rev.* 59, 617-630.

Caira, M.R., 1992. Molecular complexes of sulphonamides 2. 1:1 complexes between drug molecules: Sulfadimidine-acetylsalicylic acid and sulfadimidine-4-aminosalicylic acid. *J. Crystallogr. Spectrosc. Res.* 22, 193-200.

Caira, M.R., 2007. Sulfa drugs as model cocrystal formers. *Mol. Pharm.* 4, 310-316.

Chadha, R., Saini, A., Arora, P., Bhandari, S., 2012. Pharmaceutical cocrystals: a novel approach for oral bioavailability enhancement of drugs. *Crit. Rev. Ther. Drug Carrier Syst.* 29, 183-218.

Chen, G., Xia, M., Lei, W., Wang, F., Gong, X., 2013. A study of the solvent effect on the morphology of RDX crystal by molecular modeling method. *J. Mol. Model.* 19, 5397-5406.

Curtin, V., Amharar, Y., Hu, Y., Erxleben, A., McArdle, P., Caron, V., Tajber, L., Corrigan, O.I., Healy, A.M., 2013. Investigation of the capacity of low glass transition temperature excipients to minimize amorphization of sulfadimidine on comilling. *Mol. Pharm.* 10, 386-396.

D'Arcy D, M., Persoons, T., 2011. Mechanistic modelling and mechanistic monitoring: simulation and shadowgraph imaging of particulate dissolution in the flow-through apparatus. *J. Pharm. Sci.* 100, 1102-1115.

Darwish, E.S., Abdel Fattah, A.M., Attaby, F.A., Al-Shayea, O.N., 2014. Synthesis and Antimicrobial Evaluation of Some Novel Thiazole, Pyridone, Pyrazole, Chromene, Hydrazone Derivatives Bearing a Biologically Active Sulfonamide Moiety. *Int. J. Mol. Sci.* 15, 1237-1254.

Dea-Ayuela, M.A., Castillo, E., Gonzalez-Alvarez, M., Vega, C., Rolon, M., Bolas-Fernandez, F., Borrás, J., Gonzalez-Rosende, M.E., 2009. In vivo and in vitro anti-leishmanial activities of 4-nitro-N-pyrimidin- and N-pyrazin-2-ylbenzenesulfonamides, and N2-(4-nitrophenyl)-N1-propylglycinamide. *Bioorg. Med. Chem.* 17, 7449-7456.

Donnay, J.D.H., Harker, D., 1937. A new law of crystal morphology extending the law of Bravais. *Am. Mineral.* 22, 446-467.

Grossjohann, C., 2013. Doctoral Thesis: Pharmaceutical cocrystals: A contribution to fundamental studies addressing solubility, dissolution, formation and characterisation. 73-82.

Grossjohann, C., Serrano, D.R., Paluch, K.J., O'Connell, P., Vella-Zarb, L., Manesiotis, P., McCabe, T., Tajber, L., Corrigan, O.I., Healy, A.M., 2015. Polymorphism in sulfadimidine/4-aminosalicylic acid cocrystals: solid-state characterization and physicochemical properties. *J. Pharm. Sci.* 104, 1385-1398.

Han, J.H., Ferro, L., Vaidya, A., George, S., Pandey, A., O'Grady, D., Smith, B., 2009. A real-time study of disintegration and dissolution in solid oral dosage forms with focused beam reflectance measurement (FBRM) technology. *AAPS Journal* 11, 1162.

Hassel, R.L., Hesse, N.D., 2007. Characterization of Water Adsorption and Absorption in Pharmaceuticals TA instruments white paper 338, 1-5.

Ho, R., Naderi, M., Heng, J.Y., Williams, D.R., Thielmann, F., Bouza, P., Keith, A.R., Thiele, G., Burnett, D.J., 2012. Effect of milling on particle shape and surface energy heterogeneity of needle-shaped crystals. *Pharm. Res.* 29, 2806-2816.

Huovinen, P., Sundstrom, L., Swedberg, G., Skold, O., 1995. Trimethoprim and sulfonamide resistance. *Antimicrob. Agents Chemother.* 39, 279-289.

Larsbo, M., Fenner, K., Stoob, K., Burkhardt, M., Abbaspour, K., Stamm, C., 2008. Simulating sulfadimidine transport in surface runoff and soil at the microplot and field scale. *J. Environ. Qual.* 37, 788-797.

Legrand, M., Lecuona, A., Nogueira, J., Forte, R., 2014. Single camera 3-D shadowgraphy system for droplet sizing. 17th International Symposium on Applications of Laser Techniques to Fluid Mechanics Lisbon, Portugal, 07-10 July.

Lover, M.J., 1987. Use of 4-aminosalicylic acid as an anti-inflammatory agent. EP 0062000 B1 Patent.

Miroshnyk, I., Mirza, S., Sandler, N., 2009. Pharmaceutical co-crystals-an opportunity for drug product enhancement. *Expert Opin. Drug Deliv.* 6, 333-341.

Mirza, S., Miroshnyk, I., Heinamaki, J., Antikainen, O., Rantanen, J., Vuorela, P., Vuorela, H., Yliruusi, J., 2009. Crystal morphology engineering of pharmaceutical solids: tableting performance enhancement. *AAPS PharmSciTech.* 10, 113-119.

Mugheirbi, N.A., Paluch, K.J., Tajber, L., 2014. Heat induced evaporative antisolvent nanoprecipitation (HIEAN) of itraconazole. *Int. J. Pharm.* 471, 400-411.

Murikipudi, V., Gupta, P., Sihorkar, V., 2013. Efficient throughput method for hygroscopicity classification of active and inactive pharmaceutical ingredients by water vapor sorption analysis. *Pharm. Dev. Technol.* 18, 348-358.

Paluch, K.J., McCabe, T., Muller-Bunz, H., Corrigan, O.I., Healy, A.M., Tajber, L., 2013a. Formation and physicochemical properties of crystalline and amorphous salts with different stoichiometries formed between ciprofloxacin and succinic acid. *Mol. Pharm.* 10, 3640-3654.

Paluch, K.J., Tajber, L., Corrigan, O.I., Healy, A.M., 2013b. Impact of alternative solid state forms and specific surface area of high-dose, hydrophilic active pharmaceutical ingredients on tableability. *Mol. Pharm.* 10, 3628-3639.

Panigrahi, P.K., Muralidhar, K., 2012. Chapter 2 Laser Schlieren and Shadowgraph, Schlieren and Shadowgraph Methods in Heat and Mass Transfer. *SpringerBriefs in Thermal Engineering and Applied Science*, pp. 23-46.

Qiao, N., Li, M., Schindwein, W., Malek, N., Davies, A., Trappitt, G., 2011. Pharmaceutical cocrystals: an overview. *Int. J. Pharm.* 419, 1-11.

Ruiz, H.K., Serrano, D.R., Dea-Ayuela, M.A., Bilbao-Ramos, P.E., Bolas-Fernandez, F., Torrado, J.J., Molero, G., 2014. New amphotericin B-gamma cyclodextrin formulation for topical use with synergistic activity against diverse fungal species and *Leishmania* spp. *Int. J. Pharm.* 473, 148-157.

Serrano, D.R., Gallagher, K.H., Healy, A.M., 2015a. Emerging Nanonisation Technologies: Tailoring Crystalline Versus Amorphous Nanomaterials. *Curr. Top. Med. Chem.* 15, 2327-23240.

Serrano, D.R., O'Connell, P., Paluch, K.J., Walsh, D., Healy, A.M., 2015b. Cocrystal habit engineering to improve drug dissolution and alter derived powder properties. *J. Pharm. Pharmacol.* *In press*.

Serrano Lopez, D.R., Lalatsa, A., 2013. Peptide pills for brain diseases? Reality and future perspectives. *Ther. Deliv.* 4, 479-501.

Sobarzo-Sanchez, E., Bilbao-Ramos, P., Dea-Ayuela, M., Gonzalez-Diaz, H., Yanez, M., Uriarte, E., Santana, L., Martinez-Sernandez, V., Bolas-Fernandez, F., Ubeira, F.M., 2013. Synthetic oxoisoaporphine alkaloids: in vitro, in vivo and in silico assessment of antileishmanial activities. *PLoS One* 8, e77560.

Sugano, K., 2008. Theoretical comparison of hydrodynamic diffusion layer models used for dissolution simulation in drug discovery and development. *Int. J. Pharm.* 363, 73-77.

Sun, J., 2011. The Use of Dynamic Vapor Sorption Method in the Determination of Water Sorption Limit and Setting Specification for Drug Substance. *American Pharmaceutical Review* 14.

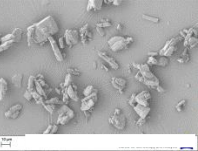
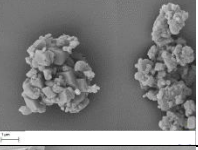
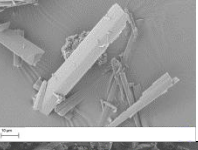
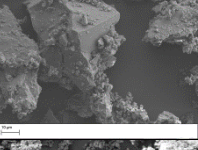
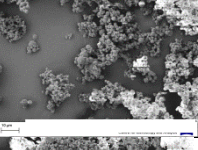
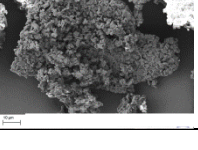
USP, 2008. United States Pharmacopeia and National Formulary, United States Pharmacopeial Convention Inc., Rockville, MD, USA, 26th Edition.

Waring, M.J., Arrowsmith, J., Leach, A.R., Leeson, P.D., Mandrell, S., Owen, R.M., Pairaudeau, G., Pennie, W.D., Pickett, S.D., Wang, J., Wallace, O., Weir, A., 2015. An analysis of the attrition of drug candidates from four major pharmaceutical companies. *Nat. Rev. Drug Discov.* 14, 475-486.

Wolfgang, M., 2011. Shadowgraph technique DOI: 10.1615/AtoZ.s.shadowgraph_technique. *Thermopedia*.

Zidan, A.S., Rahman, Z., Khan, M.A., 2010. Online monitoring of PLGA microparticles formation using Lasentec focused beam reflectance (FBRM) and particle video microscope (PVM). *AAPS Journal* 12, 254-262.

Table 1. True density, SEM micrograph, particle size and aggregation indices of SDM: 4-ASA (1:1 molar ratio) cocrystals and PM. The aggregation indices were calculated as described in the section 2.2.2. The D_{50} (μm) liquid for SDM and 4-ASA was 34 μm and 339 μm respectively.

Sample	SEM micrograph	True Density (g/cm^3)	D_{50} (μm) solid	D_{50} (μm) liquid	AI_1	AI_2	AI_3	AI_4
PM		$1.49 \pm 1.5 \times 10^{-3}$	9.4 ± 0.5	72.6 ± 2.3	21.7 ± 1.4	2.5 ± 0.5	1.06 ± 0.02	7.72 ± 0.8
PI		$1.45 \pm 7 \times 10^{-4}$	54.1 ± 5.3	80.6 ± 1.5	0.85 ± 0.1	15.8 ± 1.3	0.19 ± 0.001	1.49 ± 0.2
PII-HI		$1.41 \pm 1.4 \times 10^{-4}$	15.7 ± 0.0	27.0 ± 4.4	0.82 ± 0.3	22.8 ± 1.5	0.22 ± 0.08	1.72 ± 0.5
PII-HII		$1.37 \pm 2.1 \times 10^{-3}$	60.5 ± 6.2	172.5 ± 5.0	2.2 ± 0.6	68 ± 3.5	1.07 ± 0.02	2.85 ± 0.3
PII-HIII		$1.41 \pm 1.9 \times 10^{-3}$	5.7 ± 0.7	1042.3 ± 11.6	2.8 ± 0.5	72.1 ± 4.5	0.92 ± 0.01	182 ± 2.6
PII-HIV		$1.41 \pm 1.1 \times 10^{-3}$	24.8 ± 2.5	122.7 ± 8.6	0.82 ± 0.2	3.49 ± 0.6	0.65 ± 0.12	4.94 ± 0.7

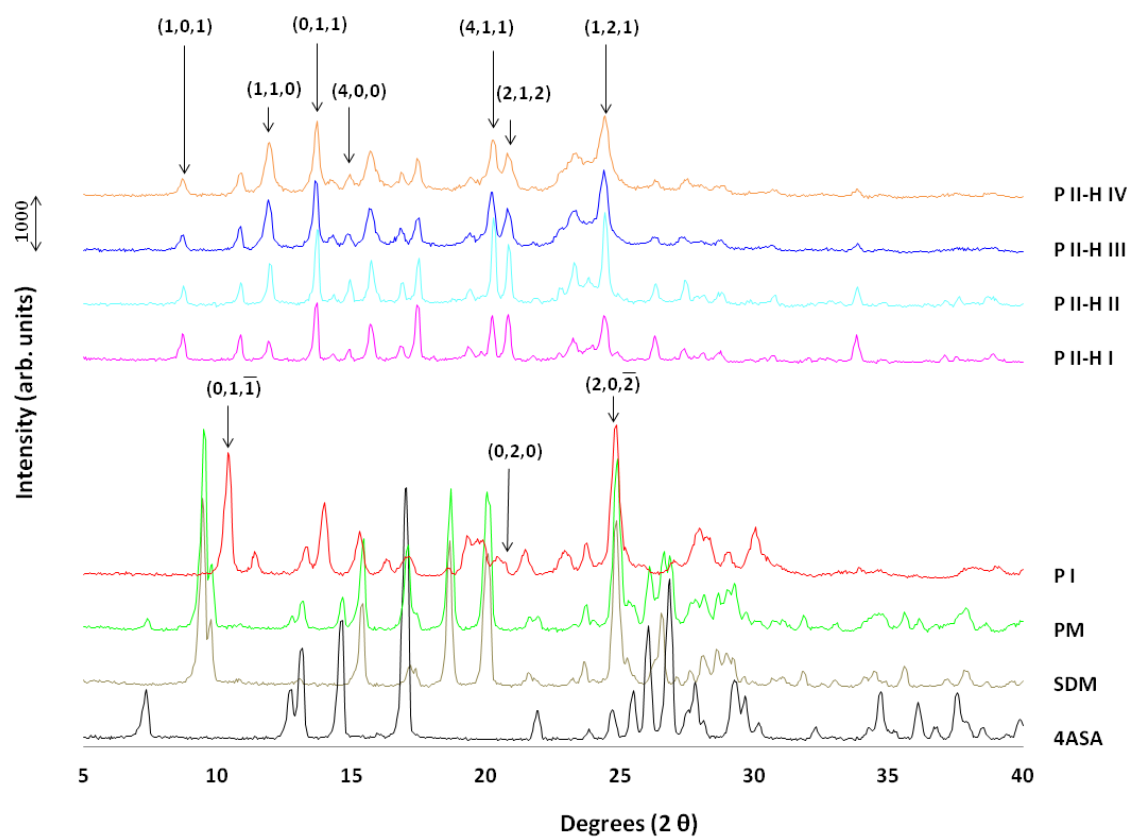


Figure 1

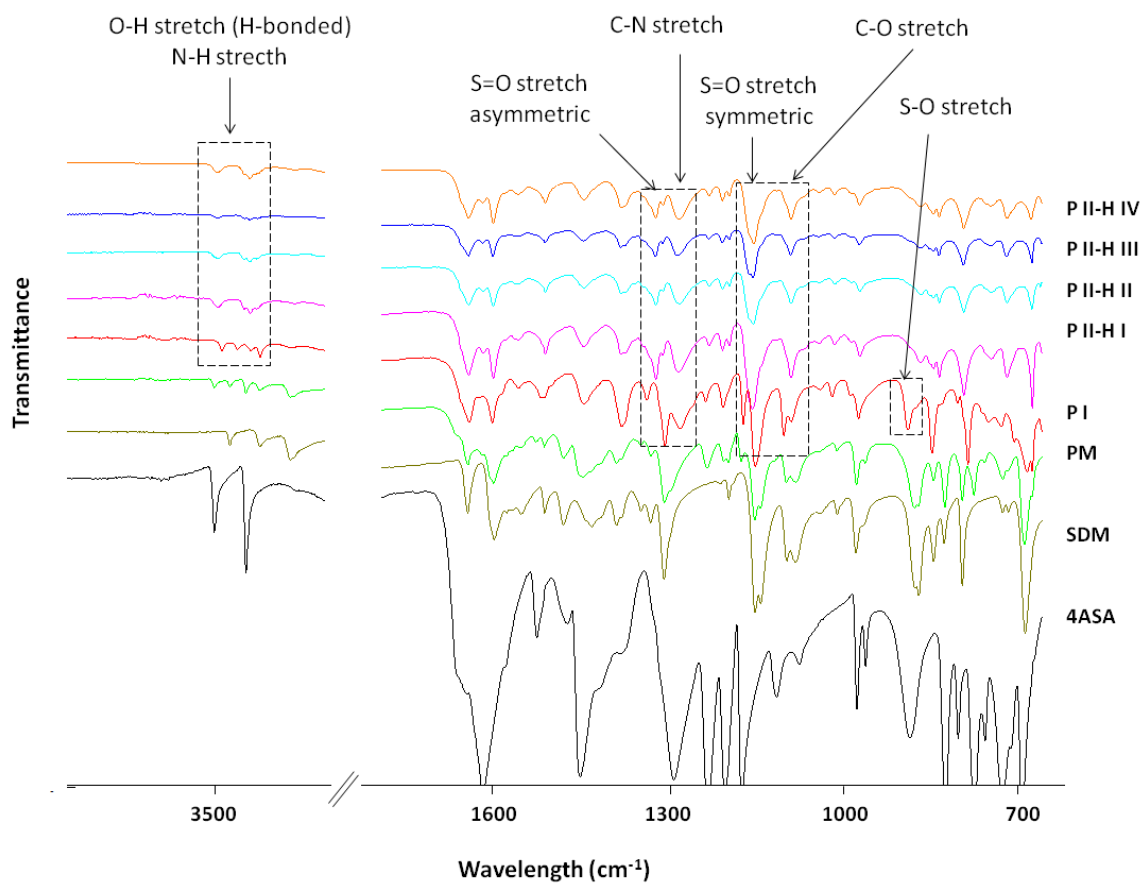


Figure 2

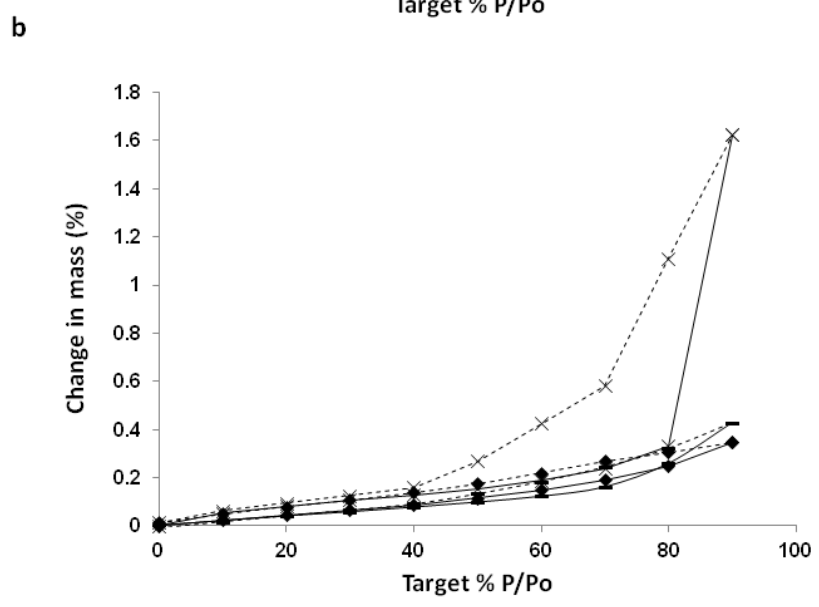
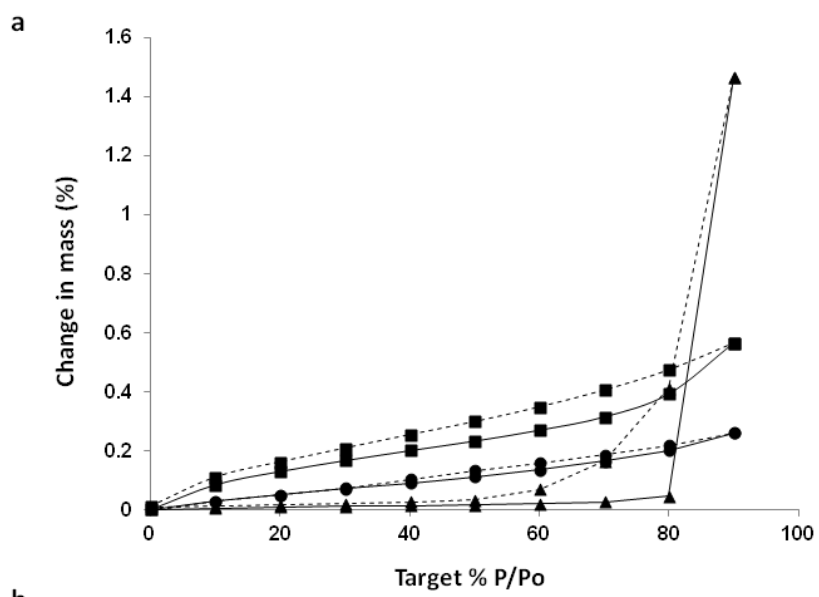


Figure 4

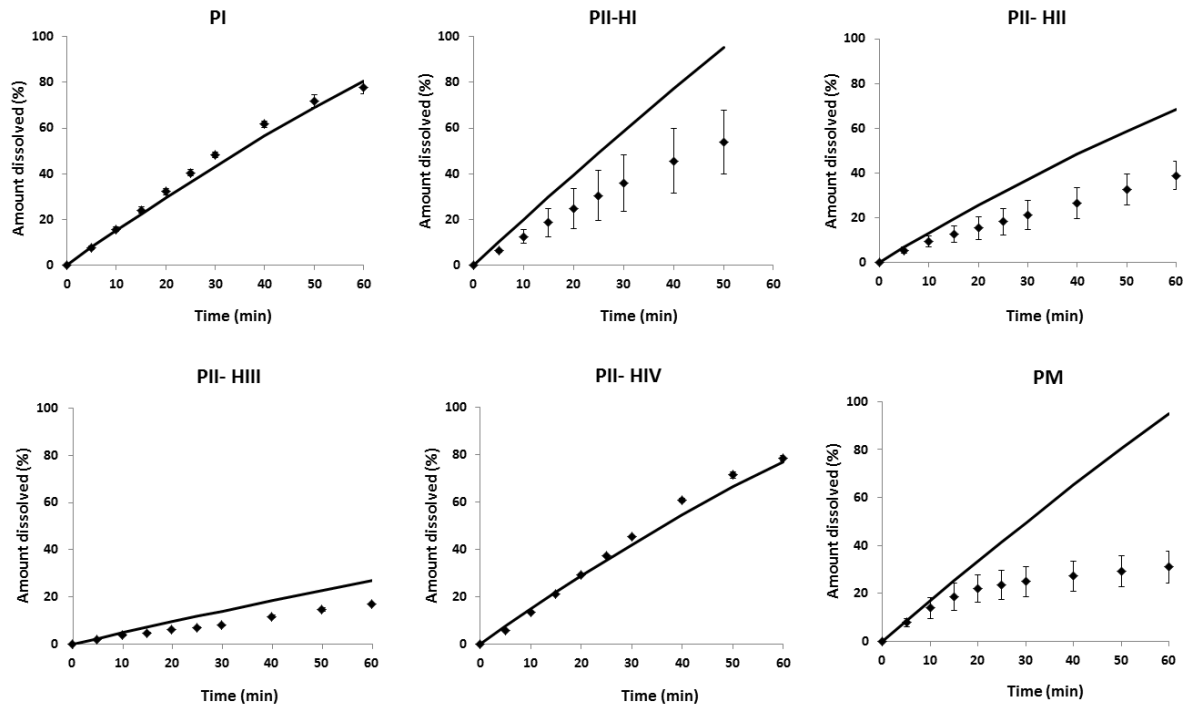


Figure 5

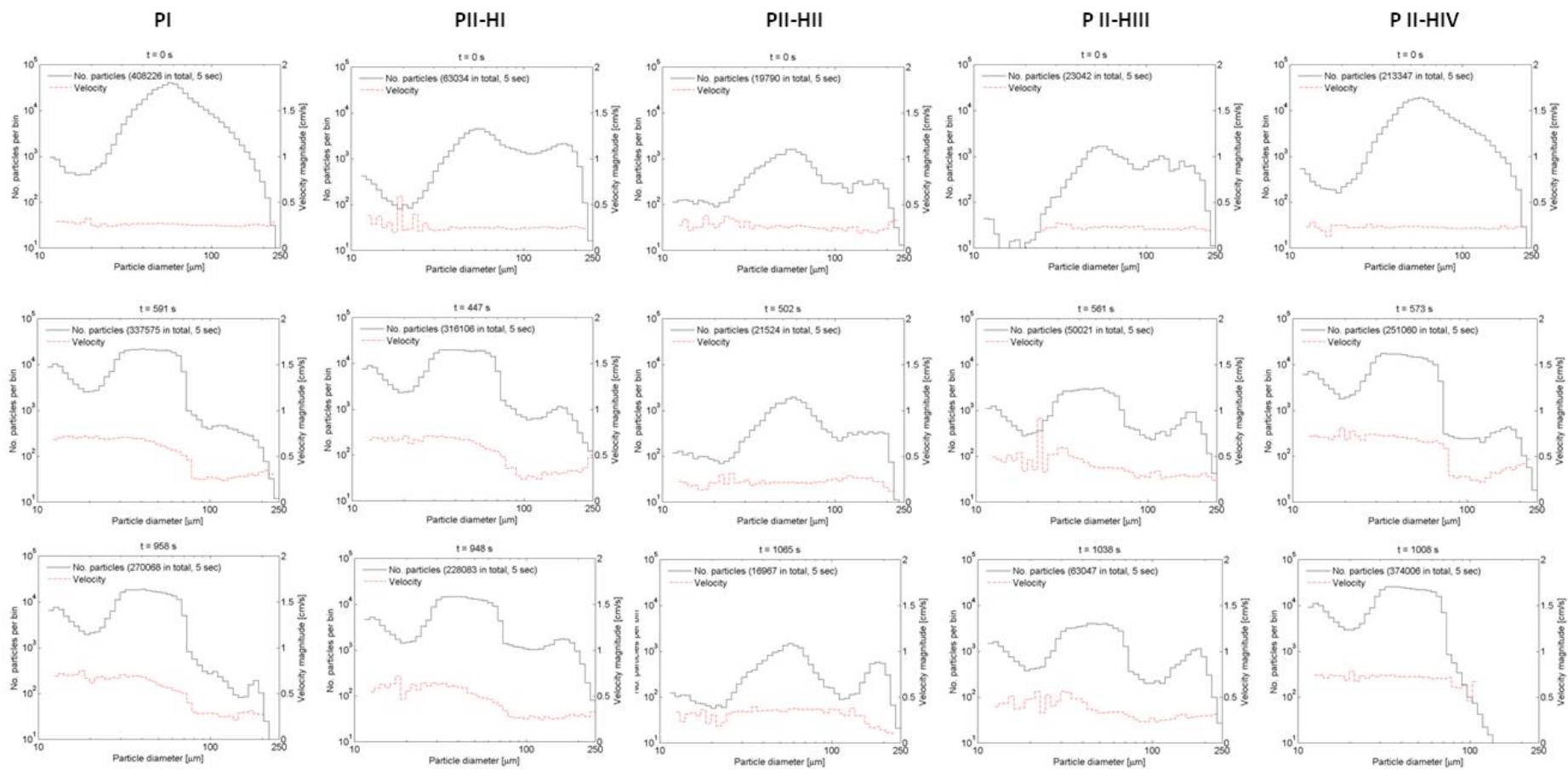


Figure 6

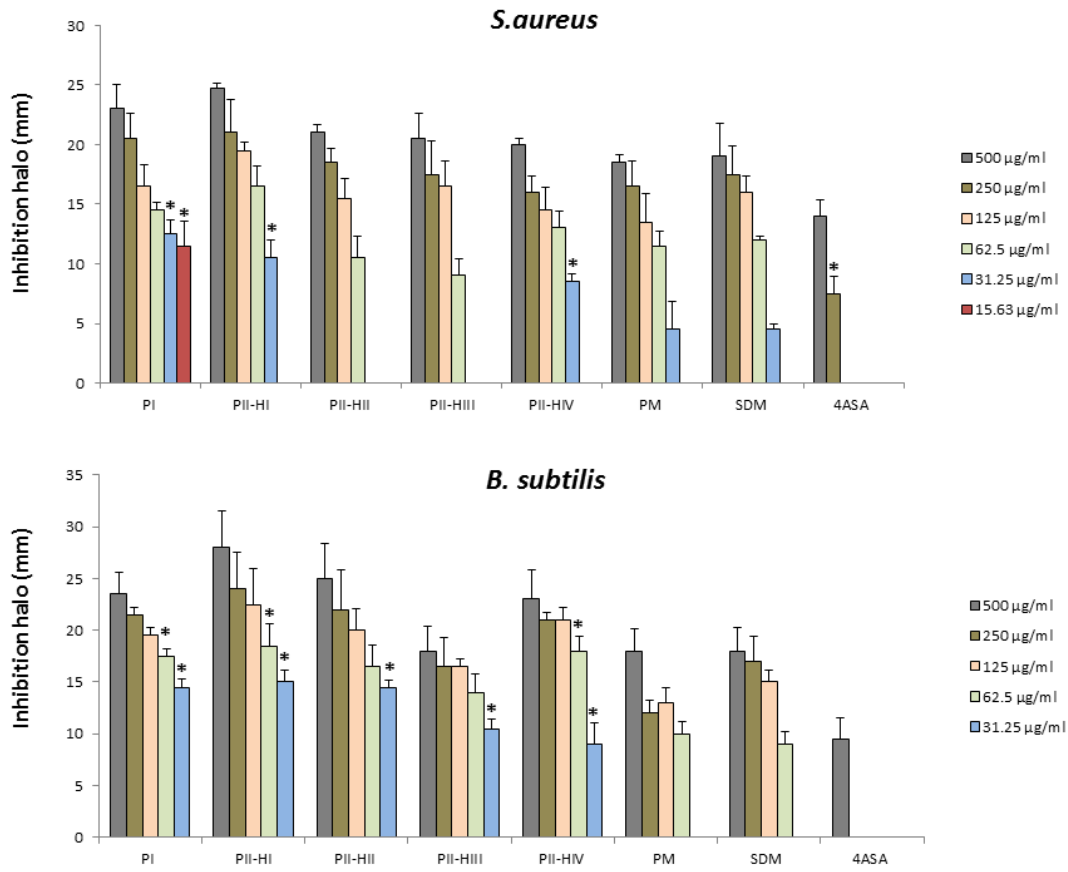


Figure 7

1 **Supplementary material**

2

3 **Modelling and Shadowgraph Imaging of Cocrystal Dissolution and Assessment of *In***
4 ***Vitro* Antimicrobial Activity for Sulfadimidine/4-Aminosalicylic Acid Cocrystals**

5

6

7 Dolores. R. Serrano¹, Tim Persoons², Deirdre M. D’Arcy¹, Carolina Galiana³, Maria
8 Auxiliadora Dea-Ayuela³, Anne Marie Healy^{1,*}

9

10

11
12 ¹School of Pharmacy and Pharmaceutical Sciences, Trinity College Dublin, Dublin 2, Ireland.

13 ²Department of Mechanical and Manufacturing Engineering, Trinity College Dublin, Dublin 2, Ireland.

14 ³Departamento de Farmacia, Facultad de Ciencias de la Salud, Universidad Cardenal Herrera-CEU,
15 Moncada, Valencia, 46113, Spain.

16

17

18

19
20 *Corresponding author:

21 Tel.: +353 1 896 1444; fax: +353 1 896 2810.

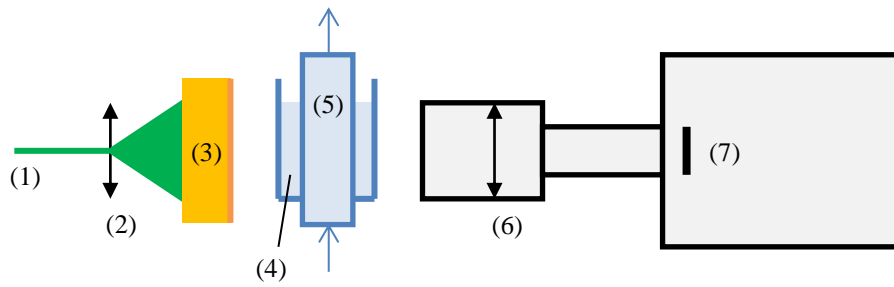
22 E-mail address: healyam@tcd.ie (A.M. Healy)

23

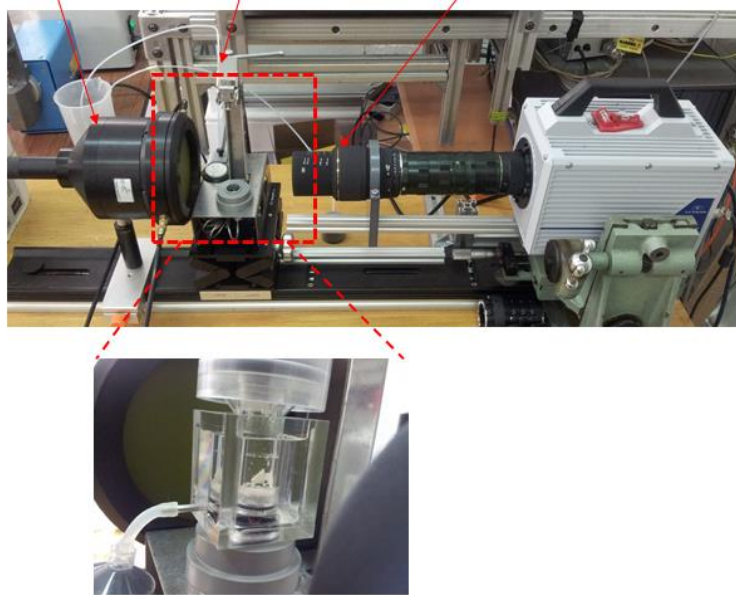
24

25

26



1



2

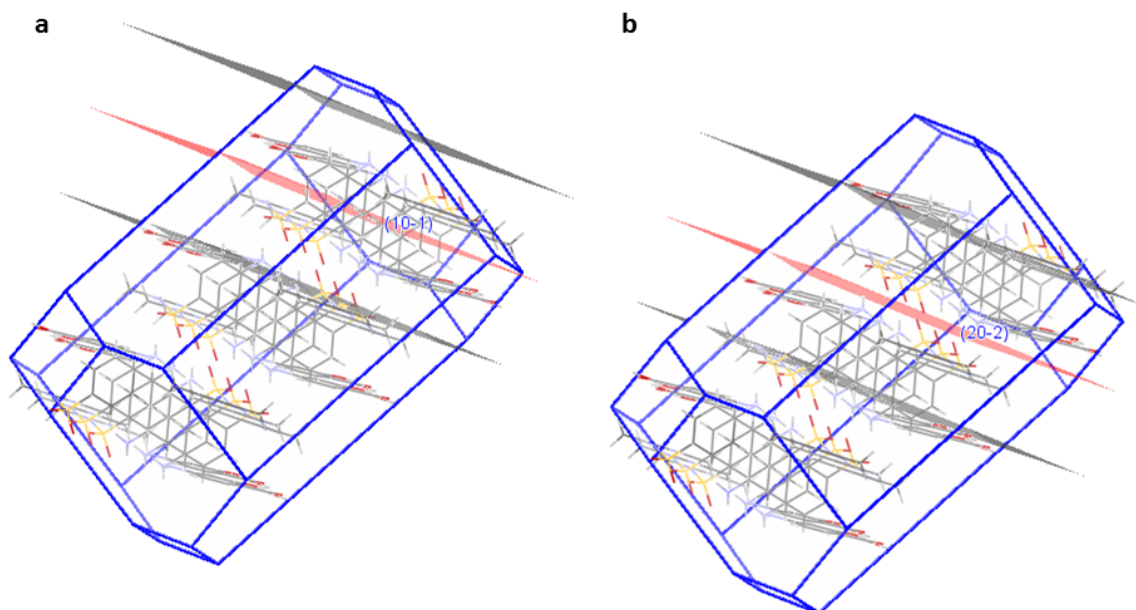
3 **Figure S1. Setup for shadowgraph imaging with a laser beam and dye diffuser creating a**
 4 **pulsed uniform background illumination behind the flow cell facility to a double-frame**
 5 **camera with high magnification lens that captures digital images of the particle-laden**
 6 **fluid. Key: (1: laser beam, 2: beam expander, 3: rhodamine-B fluorescent dye diffuser, 4: water**
 7 **jacket, 5: test cell, 6: lens arrangement, 7: CMOS high speed camera).**

8

9

10

11



1

2 **Figure S2. Visualization of crystal structure (predicted BFDH morphology) and**
3 **molecular surface packing of PI using Mercury 3.5.1. software. Key: a) visualization of**
4 **molecular surface packing along with surface chemistry of (10-1) facet and b) visualization of**
5 **molecular surface packing along with surface chemistry of (20-2) facet.**

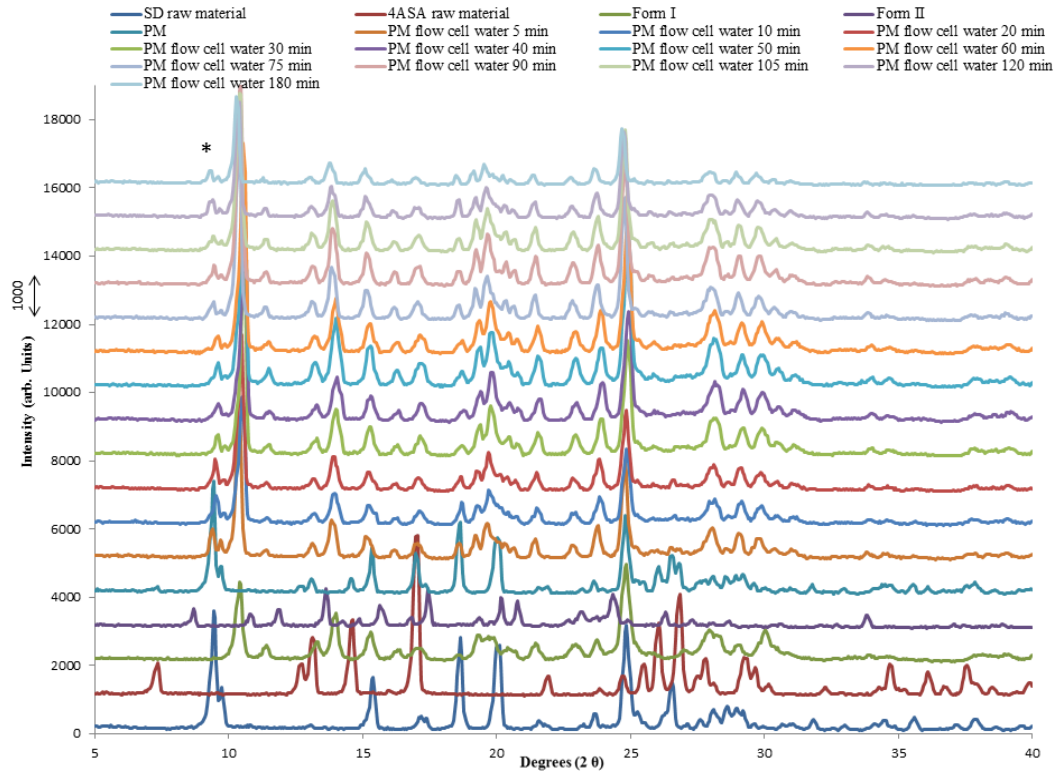
6

7

8

9

10

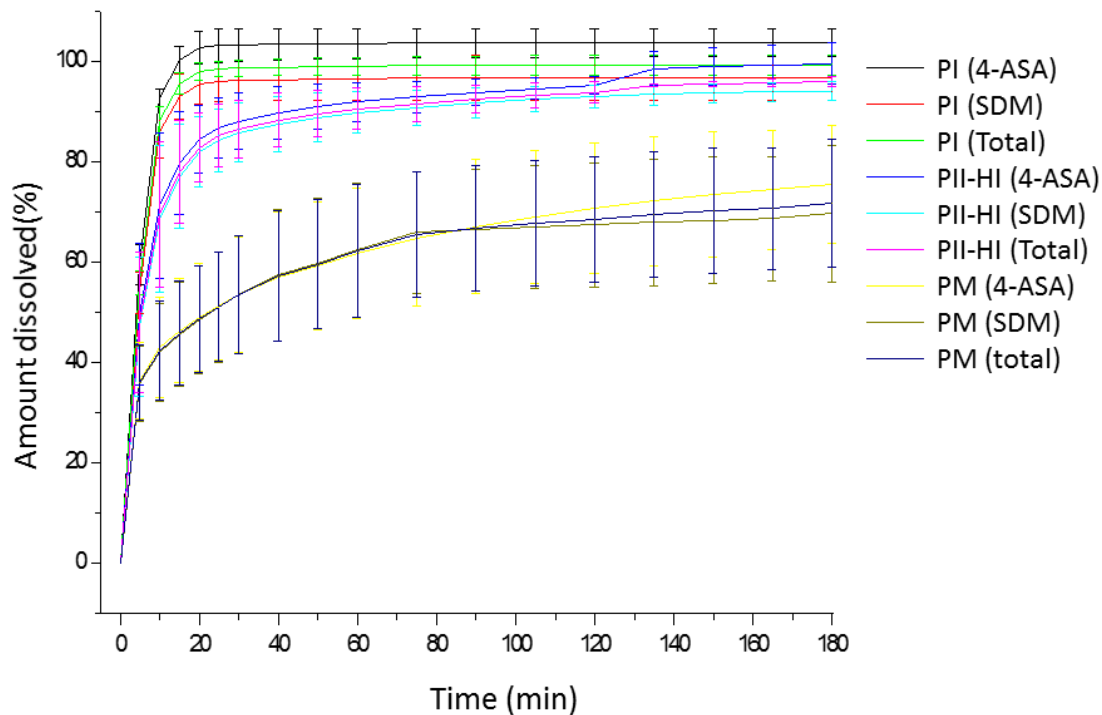


1

2 **Figure S3. PRXD of PM during flow through cell dissolution in deionised water (pH 5.5)**
 3 **over 180 min.**

4

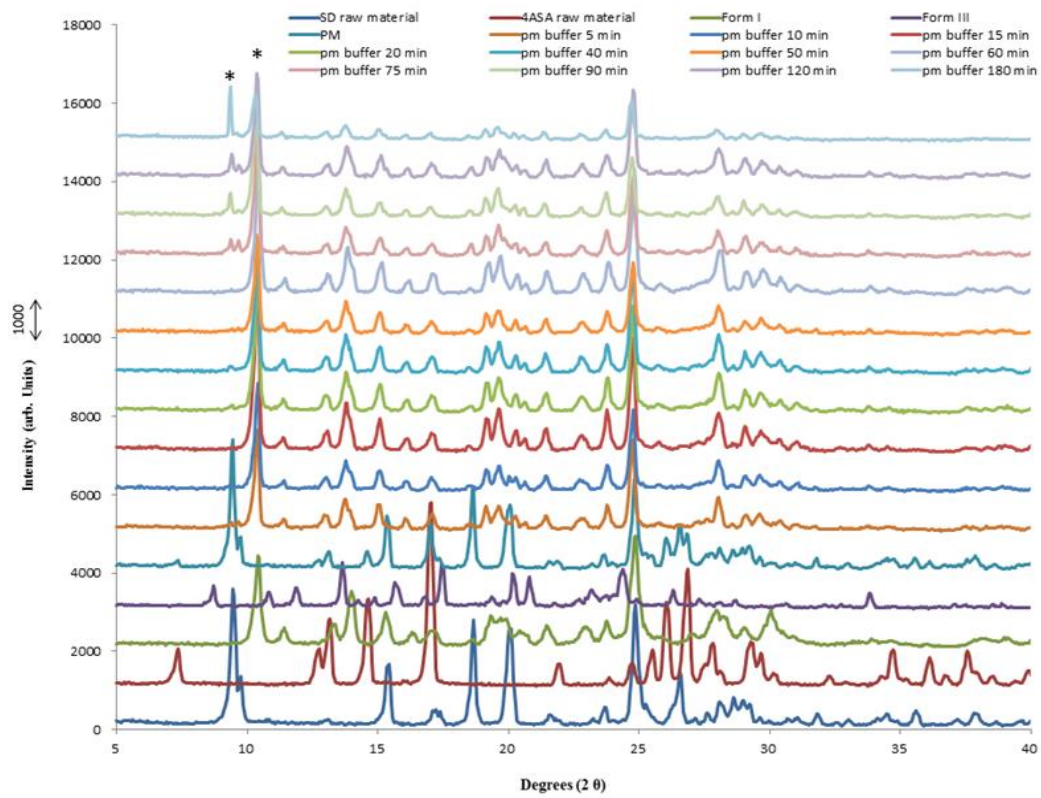
5



1

2 **Figure S4. Dissolution profiles and stoichiometry of PM, PI and PII-HI at 37°C in buffer**
 3 **(pH 1.2 from 0 to 60 min and pH 6.8 from 60 to 180 min). Key:** Physical mixture, SDM
 4 (brown), 4-ASA (yellow), total (SDM and 4-ASA, dark blue); PI, SDM (red), 4-ASA (black),
 5 total (SDM and 4-ASA, green); PII-HI, SDM (cyan),4-ASA (navy), total (SDM and 4-ASA,
 6 fucsia).

7



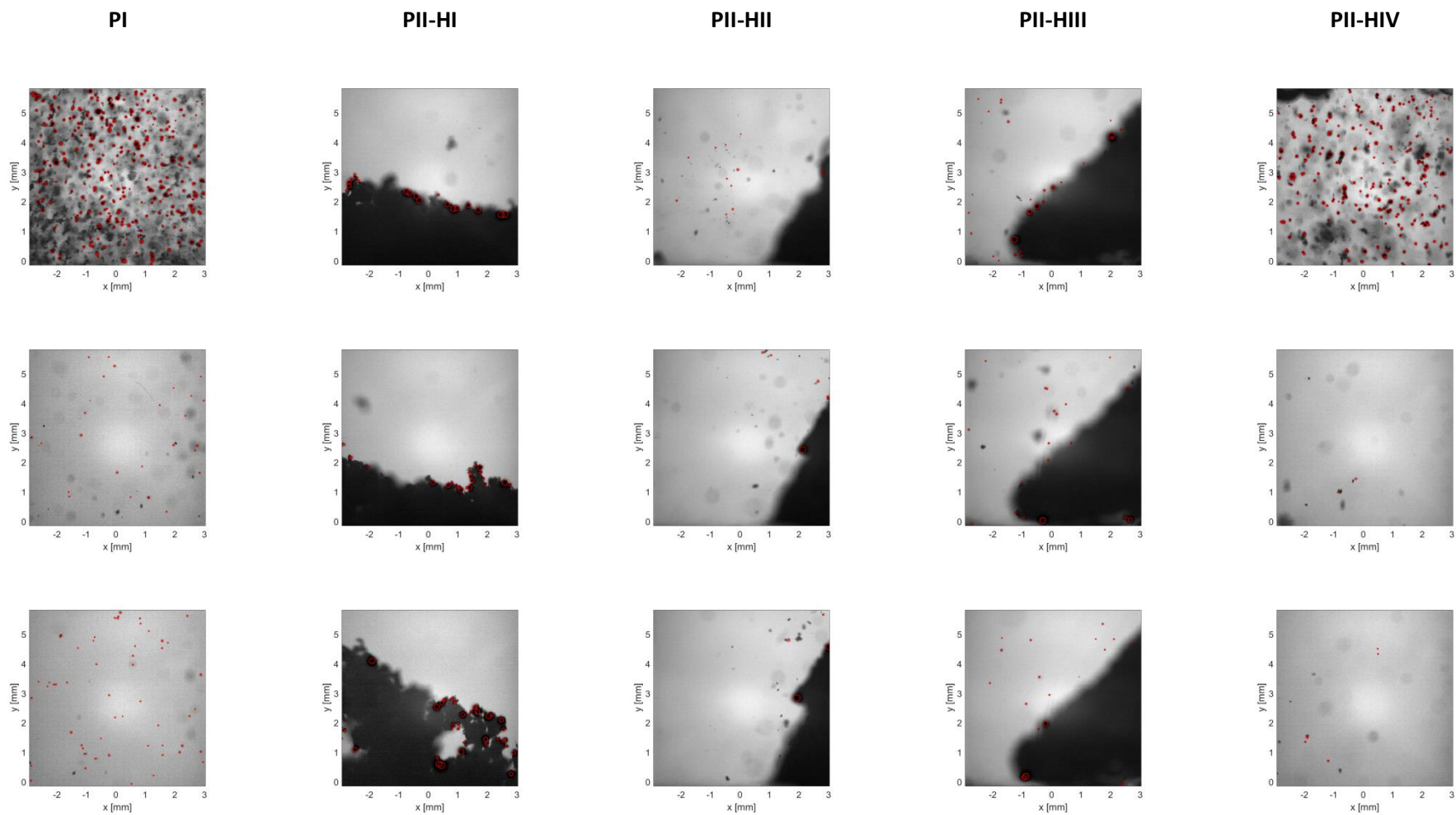
1

2 **Figure S5. PXRD of PM during flow through cell dissolution in buffer over 180 min.**

3

4

5



1

2 **Figure S6. Selected shadowgraph images at consecutive times during dissolution, with superimposed red circles representing the identified particles which have contributed to the histogram data presented**
 3 **in Fig. 6.** Data taken from 50 mg of sample in deionised water at 8 ml/min. Left to right: Data for different polymorphs/habits as indicated. Top to bottom: Selected shadowgraph images acquired at approximately $t = 0$,
 4 500, 1000 seconds of dissolution. It is worth noting the presence of a larger particle agglomerate (i.e. the large solid-looking background), with which some of the individual particles in the PII-HI, PII-HII and PII-HIII
 5 systems were associated. This observation further emphasises the aggregation behaviour present in the systems exhibiting slower dissolution.

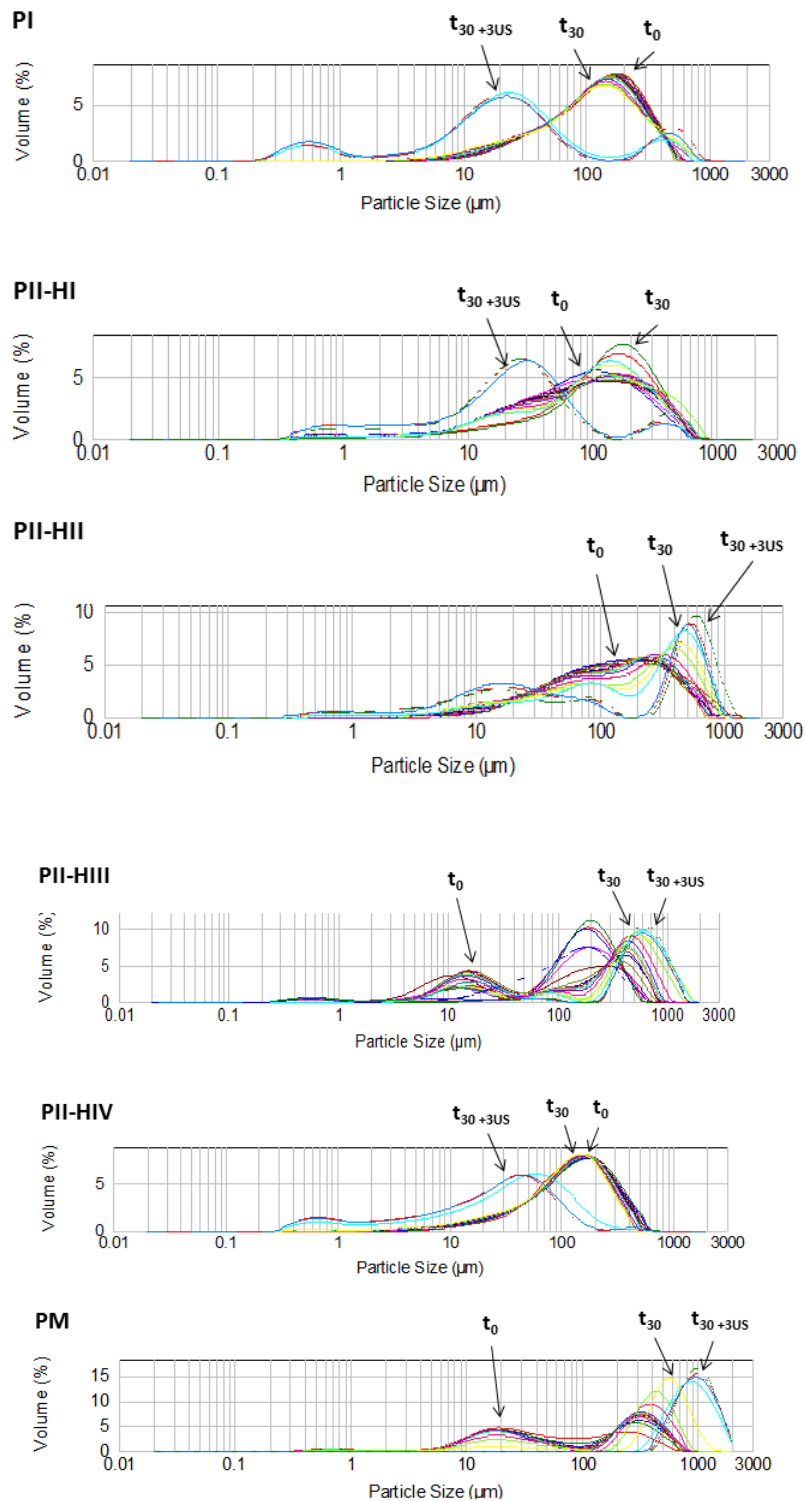


Figure S7. Monitoring of particle size distribution of concentrated systems at different time points (0, 1, 2, 3, 4, 5, 6, 7, 8, 9, 10, 15, 20, 25 and 30 min) and after three ultrasound cycles (1 min each at 80% power). Concentrated systems were generated by adding 50 mg of powder directly in the cell and keeping a constant stirring rate of 1000 rpm initially without ultrasounds. Key: t_0 is the particle size measured immediately after the powder was added on the cell under a constant stirring rate of 1000 rpm; t_{30} is the particle size 30 min after the powder was added on the cell under a constant stirring rate of 1000 rpm, t_{30+3US} is the particle size 30 min after the powder was added on the cell and after three cycles of ultrasounds at 80% power under a constant stirring rate of 1000 rpm.

